PAPER • OPEN ACCESS

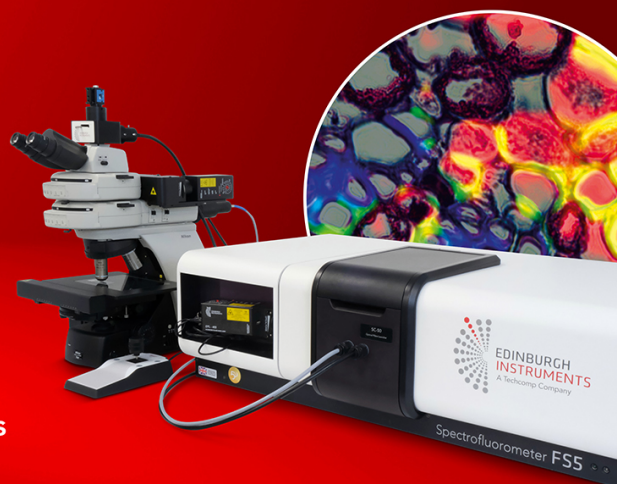# Nanoscale mapping of shifts in dark plasmon modes in sub 10 nm aluminum nanoantennas

To cite this article: Kenan Elibol *et al* 2022 *Nanotechnology* **33** 475203

View the article online for updates and enhancements.

You may also like

Nanoscale mapping of shifts in dark plasmon modes in sub 10 nm aluminum nanoantennas

Kenan Elibol[ORCID]**, Clive Downing and Richard G Hobbs**[*][ORCID]

School of Chemistry, Centre for Research on Adaptive Nanostructures and Nanodevices (CRANN) and Advanced Materials and Bio-Engineering Research Centre (AMBER), Trinity College Dublin, Dublin 2, Ireland

E-mail: hobbsr@tcd.ie

CrossMark

Abstract

In this work, we report the fabrication and spectroscopic characterization of subwavelength aluminum nanocavities—consisting of hexamer or tetramer clusters of sub 10 nm width Al nanorods—with tunable localized surface plasmon resonance (LSPR) energies on suspended SiN_x membranes. Here the volume plasmon (VP) and LSPR modes of lithographically-fabricated Al nanocavities are revealed by low-loss electron energy-loss spectroscopy (EELS) in an aberration corrected scanning transmission electron microscope (STEM). We show that the existence of grain boundaries (GBs) in these nanocavities results in shifts in the VP energy and a reduction in the VP lifetime. We map the VP energy and lifetime across GBs and we observe a decrease in VP energy and lifetime at GBs that is consistent with a reduction in free carrier density and increased plasmon scattering at these locations. Dipolar LSPR modes resonant in the UV and blue regions of the electromagnetic spectrum as well as higher-energy optically dark quadrupolar and hexapolar LSPR modes are also observed and mapped by STEM and EELS. All LSPR modes are confirmed via electromagnetic simulations based on the boundary element method. Both tetramer and hexamer structures support the excitation of dipolar bright and dipolar dark modes. Finally, we find that asymmetries in fabricated nanorod hexamer and tetramer nanocavities result in a mode mixing leading to a shift in dipolar dark LSPR modes.

Supplementary material for this article is available online

Keywords: plasmon, electron-beam lithography, electron energy-loss spectroscopy, aluminium nanoparticles

(Some figures may appear in colour only in the online journal)

1. Introduction

Plasmonic nanoparticles can amplify optical fields via excitation of localized surface plasmon resonances (LSPRs), thus providing routes to enhance energy harvesting from light [1–3], photocatalysis [4, 5], nonlinear optical processes [6, 7], optical sensing [8, 9] and optoelectronic device performance [10–12]. In the last decade, there has been an increased interest in developing plasmonic materials and devices based on more sustainable and earth-abundant materials than conventionally used noble metals [13–16]. In particular, aluminum (Al) can generate plasmon resonances across the ultraviolet (UV) region of the spectrum [4, 13, 17]. Plasmonic Al nanostructures can therefore find applications in photocatalysis and sensing where LSPRs in the nanostructures can

---

[*] Author to whom any correspondence should be addressed.

couple to electronic transitions in the UV [18–22]. In addition to these applications, the natural abundance, low cost and easy integration of Al into current semiconductor technology make it a more attractive plasmonic material than Au or Ag in terms of scalability and integration with semiconductor device processing [13, 23, 24]. Careful control of the size and position of nanoparticles within particle clusters is critical to controlling the spectral and optical-field profiles of plasmonic hotspots [25–31], which in turn determines how and where energy is transferred to neighboring materials for applications in photochemistry and optoelectronics. Fabrication of sub 10 nm structures are critical to discover new physical properties which are related to the length scale and geometry [32]. Arrays of sub 10 nm Au nanodots have previously been fabricated lithographically on ultrathin membranes, but more complex structures fabricated using the same method exhibited larger minimum dimensions [33]. Other reports of sub 10 nm structures lithographically fabricated on ultrathin membranes were typically isolated or sparse arrays of dots rather than more geometrically complex nanostructures [32]. For example, LSPRs and volume plasmons (VPs) in individual Al nanodisks with sub 10 nm dimensions have been revealed previously [34], but to date there is no report probing plasmon modes of more complex Al nanocavities consisting of clusters of sub 10 nm width nanorods. Consequently, the fabrication of nanorod clusters on ultrathin membranes with sub 10 nm feature sizes has not yet been reported.

Scanning transmission electron microscopy (STEM) and electron energy-loss spectroscopy (EELS) have been used successfully to probe and map plasmon excitations in nanoparticles and nanoparticle clusters with nanometer resolution. Moreover, STEM and EELS have also opened opportunities to probe plasmon behavior at grain boundaries (GBs) [35, 36], which is particularly relevant to plasmonic nanostructures formed from evaporated or sputtered metal films. In this work, we map both LSPR modes (dipolar and higher order polarities) and VP modes in nanorod clusters (hexamers and tetramers) fabricated by electron-beam lithography (EBL). Nanorod clusters are of significant interest for the realization of plasmonic molecules generated by strong coupling of LSPRs, tunneling devices and generation nanoscale plasmonic reactors for plasmon-enhanced photocatalysis [37–39]. We compare measured spectra to simulations and correlate shifts in energy and linewidth of VPs to GBs in these clusters of sub 10 nm width nanorods. Specifically, LSPRs in nanoparticle clusters show great promise for applications such as biosensing and detection [40–44].

Unlike dipolar bright LSPR modes, dipolar dark modes, centrosymmetric multipolar LSPRs and VPs are not typically excited by far-field plane-wave optical excitation due to symmetry restrictions and the longitudinal nature of VPs respectively [45–48]. This usually limits optical studies of plasmons in metallic nanoparticles to studies of optically-active dipolar modes rather than higher-order modes or VPs. Moreover, spatially resolved optical spectroscopic studies of plasmons are generally diffraction limited preventing interrogation on the sub 100 nm length scale [49, 50]. The spatial resolution can be enhanced to the sub 15 nm scale via scattering-type near-field scanning optical microscopy (NSOM), but techniques such as NSOM still do not provide a route to probe VPs and are complicated by the presence of the scanning tip [51]. Electron microscopes using energetic electron beams focused to sub-nanometer dimensions provide greater spatial resolution than optical microscopes [51], and also enable excitation of all LSPR modes as well as VPs [52]. As a result, EELS has become one of the most powerful methods to locally probe plasmonic properties of nanomaterials at the single particle level and at interfaces within individual particles [53, 54]. GBs represent internal interfaces within crystals and can have a significant impact on the physical properties of polycrystalline materials [55]. Lithographically fabricated plasmonic nanostructures are usually formed from polycrystalline thin films where GBs have detrimental effects on LSPR quality factors [56]. GBs can also form in sub 10 nm metal clusters, which exhibit electron-beam-induced quasi-melting during STEM imaging [57]. The energy of VPs depends strongly on charge carrier density, which can vary at GBs as has been observed previously for continuous films of Al [35, 55, 58]. Here, we present maps of VPs within clusters of ultra-small Al nanorods via EELS and reveal a strong correlation between shifts in VP energy and VP lifetime with proximity to GBs. In addition to GBs, the substrate and local environment can induce shifts in plasmon modes [59, 60]. Substrates with a finite thickness can support hybridization of plasmon modes leading to mode mixing. Since mode mixing induced by the substrate depends strongly on the thickness and dielectric properties of the substrate, mode mixing can be reduced by using thinner substrates or substrates having a lower dielectric constant [59].

In this work, we show the fabrication of clusters of sub 10 nm width Al nanorods on ultrathin SiN_x membranes. We reveal VPs and LSPRs in nanopatterned Al hexamer and tetramer nanocavities by EELS and STEM at 60 keV and we observe damping of VPs at GBs in these nanocavities. The lifetime of VPs at GBs in Al nanorods is estimated to be 352 ± 62 attosecond (as) while it is 211 ± 57 as at metal-oxide boundaries and 663 ± 43 as within the bulk Al. The structures also exhibit LSPRs including dipole, quadrupole and hexapole modes in the energy range of 2.6–6.4 eV. These LSPR modes are further studied by boundary element method (BEM) simulations of EEL spectra. Both experimental and simulated results show that the geometry of Al nanorods and the size of the central gap in the hexamer and tetramer clusters affects LSPRs. Reducing the size of the central nanogap not only changes the energy of the dipole LSPR, but also leads to splitting of the dipolar LSPR into higher (dipolar dark) and lower (dipolar bright) frequency modes [61]. These nanocavities with confined plasmonic hotspots, may be attractive for applications as nanoreactors to manipulate chemical reactions or to sense molecular systems having electronic transitions in the ultraviolet. Lastly, we propose that mode mixing induced by asymmetries in nanorod clusters (i.e. variation in nanorod width/length) leads to a shift in dipolar dark LSPR modes in Al nanocavities. Control over GBs and nanorod dimensions in Al nanorods will be key to engineering plasmonic properties on extremely short length scales and
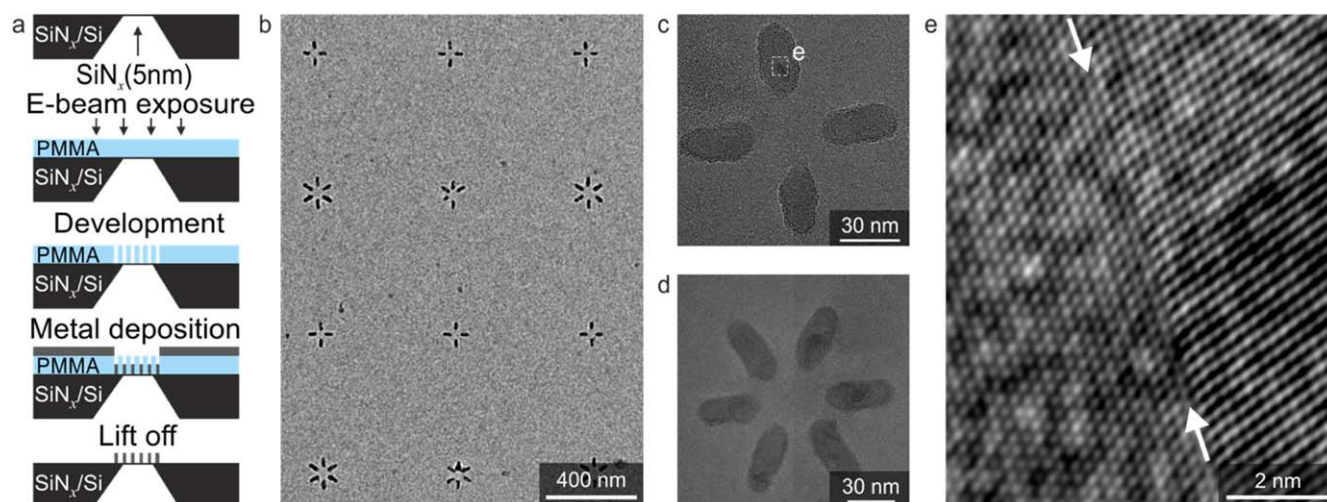
Figure 1. (a) Schematic of the sample fabrication process. Here the thickness of the SiN_x membrane, PMMA layer and Al metal are 5 nm, 70 nm, and 20 nm, respectively. (b) Bright-field TEM image of EBL-patterned nanocavities on SiN_x acquired at 200 keV. (c)–(d) Higher magnification bright field TEM images showing tetramer and hexamer Al-nanocavities shown in panel b, respectively. (e) Atomic resolution TEM image of the area in white dashed frame in panel c. The image is Wiener filtered to enhance contrast. Here the grain on the left side of the boundary line marked by arrows is rotated by 18° with respect to the grain on the right side.

may influence plasmon decay and energy transfer to surrounding media.

2. Results and discussion

The fabrication process used in this work to produce Al-nanocavities is shown schematically in figure 1(a). Here all nanocavities are fabricated on 5 nm thick SiN_x membranes by EBL (see methods section). Although EBL and focused ion beam milling with Ga^+ ions enable the production of patterned nanostructures with feature sizes as small as 10 nm, the fabrication of structures at the atomic scales is challenging using these methods [62]. Kollmann *et al* demonstrated that the combination of Ga^+ and He^+ ion milling allows fabrication of nanoscale gaps of 6 nm in Au bowties [62]. Moreover, a recent study performed by Elibol *et al* has shown that sub 5 nm gaps in Al bowties can be established via a focused electron beam in STEM [63]. Such approaches will be valuable to controlled investigations of the behaviour of plasmons at atomic-scale dimensions. Figure 1(b) displays an overview bright-field TEM image of an EBL-patterned Al nanocavity array with 600 nm spacing between neighboring nanocavities. We have fabricated two different types of nanocavity consisting of four and six Al nanorods, which we refer to as 'tetramer' and 'hexamer' nanocavities, respectively. The dimensions of nanorods in these nanocavities are approximately identical within a nanocavity, where the length, width and thickness of each nanorod, inclusive of surface oxide, are nominally 40 nm, 15 nm and 20 nm, respectively. The dimensions of the central gap of nanocavities are altered across an array by exposing PMMA with varying exposure doses during EBL thus modifying the nanorod length and central gap distance. The dose range applied during patterning was identified by fabricating Al nanocavities on bulk indium tin oxide (ITO) substrates before

fabricating nanocavities on suspended membranes (see figure S1 (available online at stacks.iop.org/NANO/33/475203/mmedia)). This approach results in larger gap sizes for nanocavities exposed at low doses and smaller gaps at higher doses. An overview of the structures fabricated on suspended SiN_x is shown in figure 1(b). Figures 1(c), (d) show higher magnification bright-field TEM images of the tetramer and hexamer nanocavities. A relatively high deposition rate (10 Å s^{-1}) was used for deposition of Al in an electron-beam evaporator to limit oxidation during metal deposition. Core-loss EEL spectra show that Al nanorods are covered with an oxide layer (see figure S2). Here, Si–L edge and N–K edge peaks, which correspond to the ionization energies of K- and L-shells in Si and N [64], are associated with the SiN_x membrane supporting the nanocavities while the O–K edge results from the ionization of the K-shell in O present in the surface oxide of the Al nanorods and any surface oxide layer formed on the SiN_x membrane. The metallic core of the Al nanorods has a width measuring <10 nm and high-resolution TEM images confirm the presence of GBs as shown in figure 1(e). Here the out-of-plane orientation of Al on SiN_x is $\langle 111 \rangle$ and the grain boundary is along the $[1\bar{2}\ 1]$ plane (see figure S3).

Figures 2(a), (b) show HAADF-STEM images of a hexamer nanocavity and the corresponding EEL spectra recorded through one of the nanorods in this hexamer (see also figure S4), respectively. The EEL spectra of nanocavities have been acquired by STEM operating at 60 keV (see methods section). As shown in the EEL spectra, the intensity of the VP is greatest at the center of the nanorod and lower at the edges, which is consistent with increased oxidation of Al at the poles of the nanorods and an expected reduction in Al thickness toward the poles [65]. The map of VP peak amplitude is superimposed on corresponding HAADF image (see figure 2(c)). To minimize errors in peak fitting, we use two Lorentzian curves separately for each plasmon peak, which
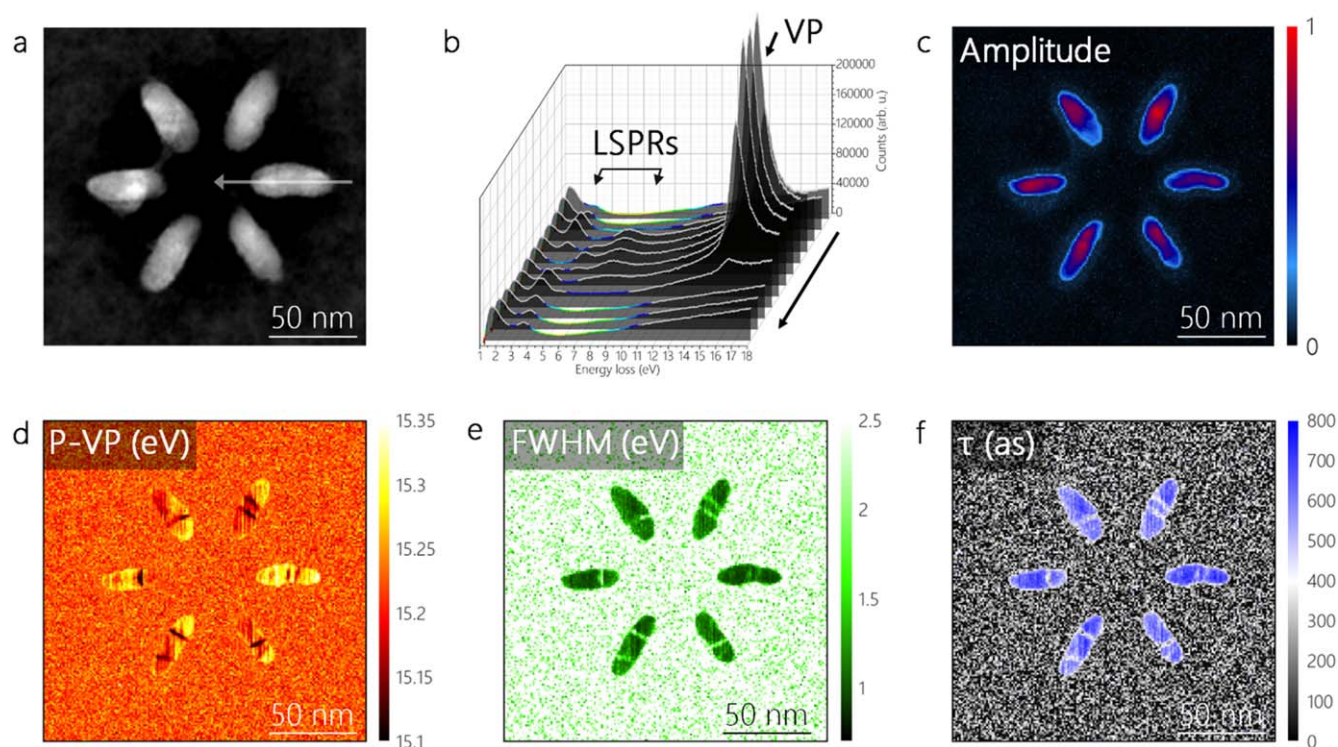
Figure 2. (a) HAADF-STEM image of a hexamer nanocavity. (b) EEL spectra collected over the white dashed line shown on HAADF image in panel (a). (c)–(f) Maps of VP peak amplitude (c), peak position (d), FWHM (e) and lifetime (f). Map of VP peak amplitude is superimposed on the HAADF image of the hexamer shown in panel (a).

are asymmetric because of the contribution of some scattering vectors [66]. The sharp VP peak in the EEL spectrum at ∼15 eV is associated with metallic Al, consequently, VP maps indicate where metallic Al is present in the nanoparticles (see the superimposed HAADF and VP map in figure 2(c)) and enable accurate measurement of the gap size of Al nanocavities (e.g. gap is ∼50 nm for the hexamer shown in figure 2(a)). As shown in figure 2(c), the amplitude of the VP spectral peak varies across the Al nanorod with larger intensities observed near the centre of the nanorods. This variation in VP intensity may be attributed to a variation in Al thickness across the nanorod, but may also be attributed to the boundary effect whereby the VP resonance is modified due to interaction with LSPRs. Here the boundary between metallic Al and the oxide layer is identified from the superimposed HAADF image and VP map (see figure 2(c)). The boundary effect results in a variation of VP intensity on the metal side of the metal-oxide boundary within a threshold distance defined by Bohr's delocalization distance given by $b_{max} = v/\omega_p$ [67]. Here the velocity of the incident electron (v) is 1.34×10^8 m s^{-1} at the acceleration voltage of 60 keV and the angular frequency of the VP ω_p is ∼15 eV. In this case, the threshold distance b_{max} is found to be 5.9 nm. As expected, the intensity of the VP doesn't saturate along the width of nanorods, which is $<2b_{max}$ (see the amplitude of VP in figure 2(c)). Interestingly, there is also not a clear saturation in the VP intensity along the length of nanorods which is longer than $2b_{max}$ (see figures 2(a)–(c)). This may be due to variation in rod width along the length of individual rods as well as thickness variations. The surface oxide thickness on

Al has been found to be ∼2 nm thick by measuring the difference between the VP map and the HAADF image of the hexamer. While the amplitude of the VP peak depends on the thickness of the Al metal, GBs in the metal result in both damping of the VP and changes in the local electron density that lead to shifts in the VP energy [35, 58]. The damping of VPs at GBs can be attributed to increased electron scattering at GBs that result in broadening of the VP peak in the EEL spectrum [68, 69]. Similar to observations in Al [35, 58], shifts in plasmon energies in ITO films have been attributed to a reduction of free carrier density at GBs in ITO thin films [36]. A map of the VP peak energy over an Al nanorod hexamer is shown in figure 2(d). The VP energy is observed to decrease at GBs and this decrease is represented by black lines running across the nanorods in figure 2(d). The existence of GBs at these locations has been shown previously in atomic resolution TEM images of the nanocavities (e.g. Figure 1(e)). Here we observe a decrease in the energy of the VP by ∼50 meV, which is similar to previous reports for continuous thin films [35]. Moreover, previous investigations have used shifts in VP energy to measure temperature locally within microelectronic devices [58, 70]. Local heating of the metal leads to material expansion and an associated decrease in carrier density and VP energy. Since the electron beam is scanning over the specimen, the local heating by the electron beam at GBs is considered to be negligible due to the high rate of heat conduction depending on the power of incident electron beam [71]. We thus attribute the decrease in VP energy at GBs to an intrinsic drop in carrier density at GBs in the material [72, 73]. In addition to the decrease in VP energy,

we observe an increase in the width of VP peaks at GBs as represented in the map of the full width at half maximum (FWHM) of the VP peak shown in figure 2(e). An increase in the FWHM of the VP peak at GBs is consistent with the expected increase in plasmon scattering at GBs and the associated reduction in plasmon lifetime. The lifetime (τ) of VPs in nanopatterned Al can be approximated from the spectral linewidth using the Heisenberg uncertainty relation from the expression $\tau = \hbar/\text{FWHM}$ [34]. Using this expression, the lifetime of VPs on Al nanorods in hexamer and tetramer nanocavities can be estimated as 663 ± 43 as, which is consistent with previous reports for 10 nm diameter Al nanodisks [34]. As stated above, GBs in Al nanoantennas are expected to reduce the lifetime of VPs due to carrier scattering. Here, unlike previous reports for continuous thin films, we have measured the VP lifetime in Al nanorods at the Al-AlO$_y$ interface ($\tau = 211 \pm 57$ as) and at GBs ($\tau = 352 \pm 62$ as). Our results suggest that VP damping is more pronounced at the Al-AlO$_y$ interface than at GBs and consequently routes to modify the Al-AlO$_y$ interface may be more important to improve plasmon quality factors than efforts to reduce the number of GBs. Despite the inhomogeneous intensity distribution of VPs in nanorods (figure 2(c)), the VP lifetime is relatively homogeneous in regions without GBs and metal-oxide boundaries (see figure 2(f) and figure S5).

Detailed EELS analyses for LSPRs in hexamer and tetramer Al-nanocavities are given in the supplementary information (see figures S6 and S7). The hexamer shown in figure S6(a) has LSPR modes at energies of 3.20 ± 0.03 eV, 3.69 ± 0.03 eV, 4.66 ± 0.01 eV and 6.41 ± 0.36 eV while the tetramer shown in figure S7(a) exhibits LSPRs at energies of 3.16 ± 0.01 eV, 3.73 ± 0.03 eV, 4.78 ± 0.03 eV and 6.41 ± 0.33 eV. Also notable are strong peaks at energies of $\sim$1.4 eV and $\sim$2.0 eV, which can be attributed to interband transitions in Al (yellow curves in figures S6(c) and S7(c)) and the silicon nitride substrate (orange curves in same spectra). EEL spectra with the SiN$_x$ contribution subtracted are shown in figures S6(e) and S7(e). In the 3–4 eV range, there are two dipolar LSPR modes (low and high frequency modes) with slightly different energies appearing in both Al-nanocavities. The first dipolar mode D$_B$ (low frequency mode) has a greater probability of excitation at the outer edge of the nanorods while the second dipolar mode D$_D$ (high frequency mode) is preferentially excited at the centre of the cavity, e.g. locations 3 and 1 in figures S6(a) and S7(a) respectively. The energies of those dipole LSPR modes are found to be 3.20 ± 0.03 eV and 3.69 ± 0.03 eV (for hexamer) and 3.16 ± 0.01 eV and 3.73 ± 0.03 eV (for tetramer). In addition to dipole LSPR modes, an edge LSPR mode Q arises at 4.66 ± 0.01 eV for hexamers and at 4.78 ± 0.03 for tetramers. Both dipole and quadrupole LSPR modes can be distinguished readily in the experimental data and are confirmed by BEM simulations of EEL spectra performed at a beam energy of 60 keV (see figures S6(f) and S7(f)). The last LSPR mode H appearing in both nanocavities is a hexapolar LSPR mode at 6.41 ± 0.36 eV for hexamers and at 6.41 ± 0.33 eV for tetramers. The influence of nanorod

dimensions on the LSPRs is also revealed via BEM simulations of low-loss EEL spectra in figures S8 and S9. The BEM simulations show that the energies of dipolar and quadrupolar LSPR modes increase with nanorod width up to 18 nm. Increasing nanorod length leads to shifts of all LSPR modes to lower energies. In addition, BEM simulations suggest that the thickness of nanorods has a significant effect on the energies of all LSPR modes with LSPR modes shifting to higher energies as the thickness increases. Moreover, these simulations show that the central gap size strongly influences the dipole LSPR modes in hexamers and tetramers. As the central gap size is decreased, the dipolar LSPR mode splits into higher and lower energy modes consistent with coupling of dipolar modes. Based on BEM simulations, splitting of the dipole mode emerges for gap sizes less than 58 nm (for hexamer) and 43 nm (for tetramer) with a single dipole LSPR mode observed for larger gap sizes (see figure S9). The onset of splitting of the dipole mode at larger gap distances for hexamers is consistent with stronger coupling between nanorods in clusters having this geometry. The influence of the gap size on the dipole LSPR modes has been revealed theoretically for both hexamers and tetramers (see figure S9). These results indicate that dipole LSPR modes excited inside and outside of the nanocavities split into low and high frequency modes as the gap size is reduced and coupling with neighbouring nanorods increases. This splitting of dipolar LSPRs that is predicted by BEM simulations is also observed in the experimental data (see figures S6 and S7). The splitting is clearest at beam positions 1 and 3 for the hexamer clusters where the blue and green curves in figure S6(c) represent peaks D$_B$ and D$_D$ arising due to splitting of the dipole LSPR. The energy splitting range of dipole LSPR modes in hexamers is larger compared to tetramers for similar gap sizes (figure S9). Unlike the dipole LSPR mode, the energies of quadrupole and hexapole LSPR modes appear to be independent of gap size for the tetramer clusters. However, BEM simulations (figure S9) suggest that the quadrupole mode in hexamer clusters also splits into lower and higher frequency modes at smaller gaps sizes than those experimentally studied here. This splitting can be seen for the peak at 5 eV in the spectra modeled at position 3 in the hexamer clusters in figure S9(b).

Maps of LSPR modes in hexamer and tetramer Al-nanocavities were extracted from spectrum images at EEL values associated with the corresponding LSPRs as shown in figures 3(a) and 4(a). As discussed earlier, low and high frequency dipole LSPR modes are observed in both hexamer and tetramer Al nanocavities and these modes are excited at position 3 (at 3.20 ± 0.03 eV for hexamer and at 3.16 ± 0.01 eV for tetramer) and position 1 (at 3.69 ± 0.03 eV for hexamer and at 3.73 ± 0.03 eV for tetramer) respectively. The first two maps shown in figures 3(a) and 4(a) respectively, clearly show the distributions associated with the dipole LSPR modes excited at the outer edge (D$_B$) and the centre (D$_D$) of the nanocavities. The oxide layer covering the metallic Al nanorods is not visible in the maps shown in figure 3, but is observed in the superimposed HAADF images and VP maps in figure S10. Additional EELS maps are also
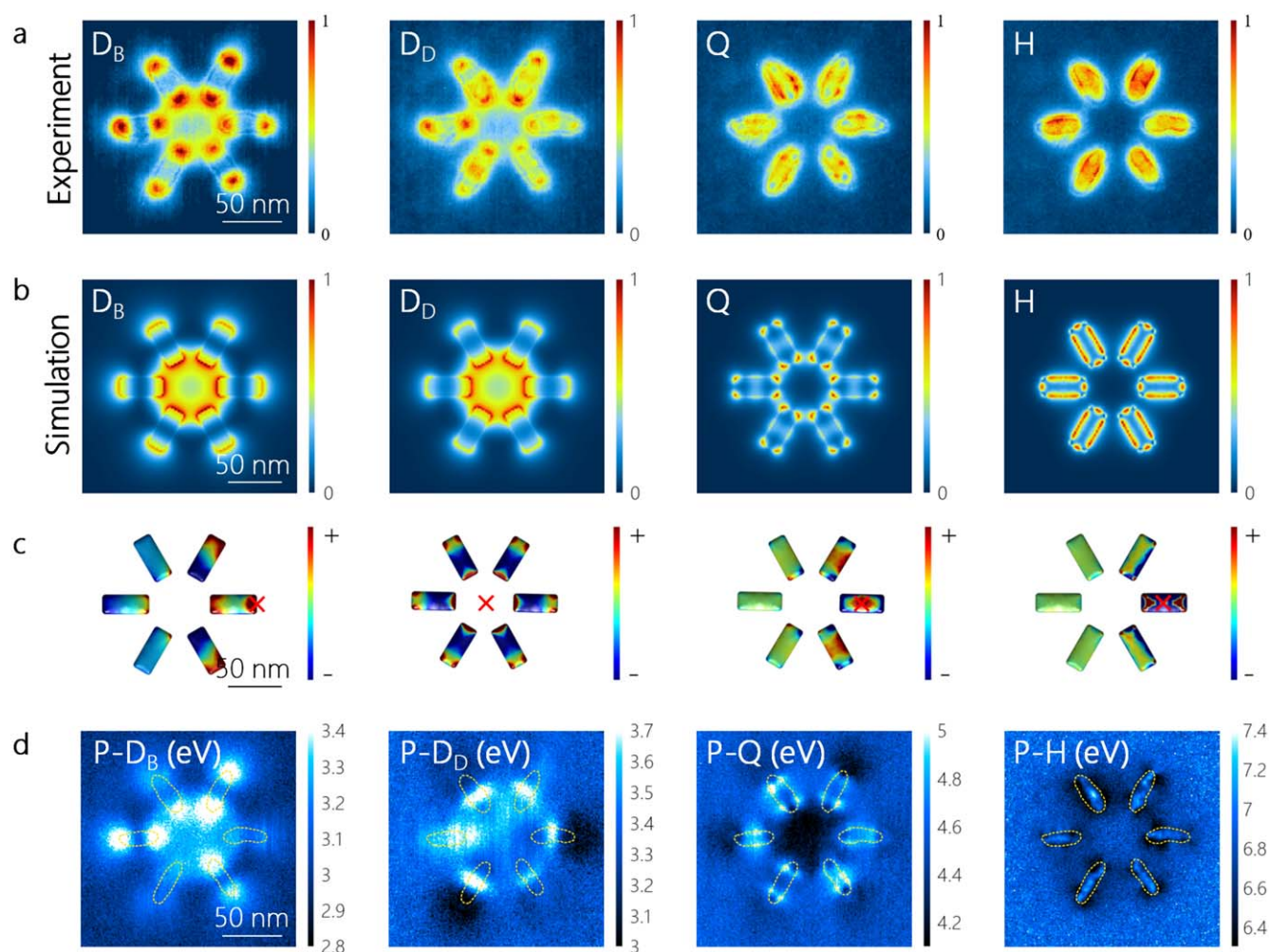
Figure 3. (a) Experimentally measured spatially resolved EELS maps of hexamer at the energy losses of 3.20 ± 0.03 eV, 3.69 ± 0.03 eV, 4.66 ± 0.01 eV, 6.41 ± 0.36 eV, respectively. (b) Corresponding simulated EELS maps at the energy losses of 3.24 eV, 3.66 eV, 5.10 eV, 6.52 eV, respectively. (c) Simulated surface charge distributions calculated by an electron beam excitation at the energies of 3.24 eV, 3.66 eV, 5.10 eV, 6.52 eV, respectively. (d) The maps of peak positions for the LSPR modes of hexamer. The yellow dashed outlines show the location of nanorods.

shown in figures S11 and S12 for hexamer and tetramer nanocavities with different gap sizes and the dipole energies of these structures are given in figure S13. As described previously, the dipole energies of these nanocavities are predicted to split into low and high frequency modes for small gap sizes (<58 nm for hexamer and <38 nm for tetramer). The simulated EEL spectra shown in figures S13(c), (d) also show that the splitting energy increases with decreasing gap size, however, simulated splitting energies differ from the experimental data. This difference might be due to the oxide layer at the surface of the nanorods leading to shifting LSPR modes relative to the simulated energies and irregularities in the shape of nanorods due to the EBL process (see figures S11 and S12). In the simulated EEL spectra shown in figure S9, the energies of quadrupole and hexapole LSPR modes in both tetramer and hexamer nanocavities are shifted with gap size. The energy shift of these higher energy LSPR modes in tetramers is however smaller than those calculated for hexamers. Additionally, the quadrupolar mode in hexamers splits into two modes for small gaps. The experimental data in

figure S14 also shows a similar trend, however the energy shifts of quadrupolar modes in tetramers and hexapolar modes in hexamers are larger compared to simulated values in figure S9. As discussed above, this is likely due to non-uniformities in the experimentally fabricated structures relative to the modeled material and the dielectric function used in BEM simulations. The simulated EELS maps corresponding to the dipolar, quadrupolar and hexapolar modes excited in nanorod clusters (see figures 3(b) and 4(b)) are in good agreement with the experimental data (see figures 3(a) and 4(a)). To further reveal the LSPR modes observed by EELS mapping, we calculated the surface charge distributions for all these LSPRs (see figures 3(c) and 4(c)). The surface charge distributions calculated by e-beam excitations show that the LSPRs excited at 3.24 eV (for hexamer) and 3.16 eV (for tetramer) are dipolar bright modes (D_B modes in figures 3(c) and 4(c)). Simulated surface charge distributions for the D_B modes under plane-wave excitation are shown in figure S15. The surface charge distribution calculated by e-beam excitation shows that the high frequency modes
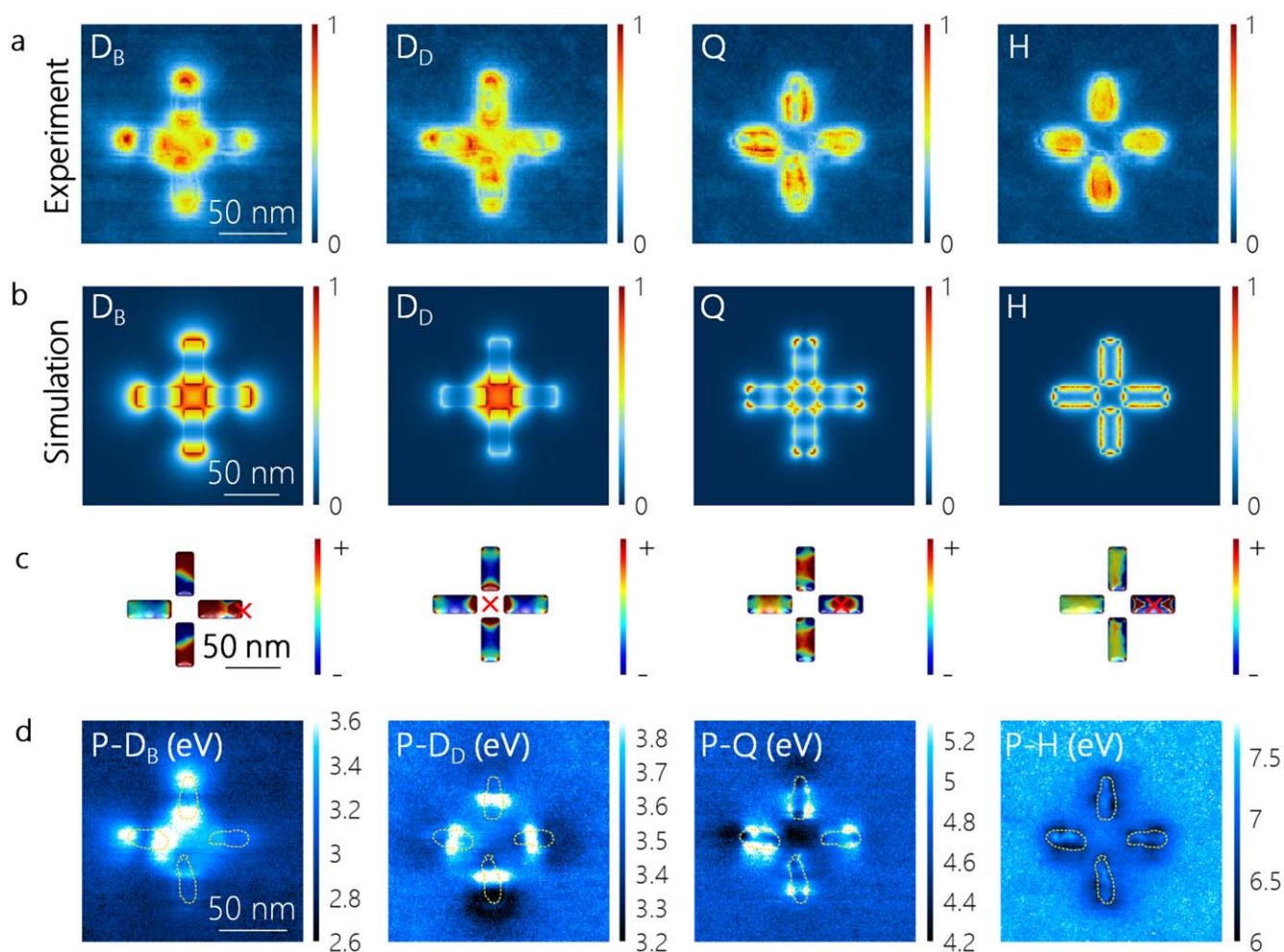
Figure 4. (a) Experimentally measured spatially resolved EELS maps of tetramer at the energy losses of 3.16 ± 0.01 eV, 3.73 ± 0.03 eV, 4.78 ± 0.03 eV, 6.41 ± 0.33 eV, respectively. (b) Corresponding simulated EELS maps at the energy losses of 3.16 eV, 3.72 eV, 5.03 eV, 6.56 eV, respectively. (c) Simulated surface charge distributions calculated by an electron beam excitation at the energies of 3.16 eV, 3.72 eV, 5.03 eV, 6.56 eV, respectively. (d) The maps of peak positions for the LSPR modes of hexamer. The yellow dashed outlines show the location of nanorods.

excited at 3.66 eV (for hexamer) and 3.72 eV (for tetramer) are dipolar dark modes (D_D). In addition to this, the simulated surface charge distribution calculated by e-beam excitation for the tetramer show the existence of both dipolar bright and dipolar dark mode excitations at 3.16 eV (see figure 4(c)). These results demonstrate that D_D modes in tetramers can be excited at the nanocavity hotspot (central gap of the nanocavity) and the poles of nanorods while the same mode is only excited within the hotspot for hexamers. Here, the D_B and D_D modes are formed due to the hybridization of dipolar modes in nanorod clusters [74]. We do not observe coupling between other higher order dark modes (Q and H). Based on simulation results shown in figure S9, we expect that smaller gap sizes below 40 nm are required to observe such mode hybridization in hexamers.

Figures 3(d) and 4(d) present the maps of peak positions (P-D_B, P-D_D, P-Q, P-H) for dipolar bright, dipolar dark, quadrupolar and hexapolar modes, respectively. Although the maps of P-D_B, P-Q and P-H are in agreement with the corresponding plasmon mode maps shown in figures 3(a) and 4(a), the P-D_D map looks quite different to the D_D mode map.

Investigating this observation, we considered the influence of variations in nanorod length on the D_D mode of the clusters. We performed EELS simulations where one of the six rods in hexamers is 10% shorter or 10% longer than the other 5 nanorods (see figure S16). Interestingly, the slight difference in one of the nanorods induces a significant change in the D_D mode while other LSPR modes remains effectively unchanged. The shift of the D_D mode in the simulations seems to be due to mode mixing induced by the asymmetry in the hexamers. Similar to the simulated EEL spectra, we observe a significant change in the D_D modes of experimental hexamer and tetramer structures, which can be attributed to asymmetries in the nanorod cluster (see figures 3(d) and 4(d)). Not only do variations in lengths and widths of nanorods cause changes in plasmon resonances, but also defects such as ridges and grooves can lead to additional surface plasmon scattering resulting in spectral shifts of LSPRs [75]. Moreover, inhomogeneous surface oxide composition and thickness can also affect LSPRs and consideration of such factors may be required to achieve improved simulations for experimentally fabricated structures.

3. Conclusions

Here we have successfully fabricated sub 10 nm width Al nanorods in clusters with different geometries (hexamer and tetramer) on suspended SiN$_x$ membranes and we have revealed their VPs and LSPRs by EELS in an aberration-corrected STEM operating at 60 keV. All measured VP and LSPR modes have been modeled and confirmed via BEM simulations of EEL spectra. Our study confirms a shift in the VP energy at GBs in Al nanorods as well as a reduction in the VP lifetime. The lifetimes of VPs at metal-oxide boundaries, GBs and within Al nanorods have been found to be 211 ± 57 as, 352 ± 62 as and 663 ± 43 as. A better understanding of plasmon behavior at GBs and metal-oxide interfaces will be key to advancing the use of plasmonic nanostructures in photocatalysis and optoelectronic devices. Our findings further show that the dipolar bright and dipolar dark LSPR modes of hexamers and tetramers can be tuned by altering the size of nanogaps and the dimensions of Al nanorods within the nanocavities via nanolithography. In addition, Al nanocavities with a gap size less than 58 nm for hexamer and 38 nm for tetramer result in energy splitting producing dipolar bright and dipolar dark LSPR modes. This leads to the production of a dipole mode in the UV and blue regions of the spectrum, which can be used for applications in plasmon-enhanced UV photochemistry. These nanopatterned UV nanocavities have the potential to be used as nanoreactors to manipulate chemical reactions within plasmonic hotspots. Lastly, we show that non-uniformities in nanocavities can lead to mode mixing inducing a shift in dipolar dark LSPR modes. Future work with plasmonic Al nanostructures should consider producing smaller antennas and engineering GBs and interfaces with oxide layers within these materials to control plasmon decay and energy transfer to the environment.

4. Methods

4.1. Sample preparation

Al nanocavities were fabricated by electron beam lithography on 5 nm thick SiN$_x$ membranes having windows measuring 50 μm $\times$ 50 μm, which were purchased from *SiMPore Inc*. Firstly, the surfaces of SiN$_x$ membranes were cleaned by oxygen plasma (*Diener Pico* 100 W, 0.3 mbar O$_2$) for 3 min. The SiN$_x$ membranes were then coated with a 70 nm thick layer of PMMA (2 wt% 950 k PMMA in anisole) by spin coating at 3 krpm (acceleration rate of 2 krpm s^{-1}) for 1 min. Following spin-coating, samples were baked on a hot plate in air at 180 $^{\circ}$C for 2 min. EBL was performed on a *Zeiss Supra* 40, using a *Raith Quantum* pattern generator, with a 7 μm objective aperture and an acceleration voltage of 20 keV. The working distance, beam current and areal dose were 4 mm, 20 pA and 1300 μC cm^{-2}, respectively. The exposed resist was then developed in 3:1 methyl isobutyl ketone (MIBK):isopropyl alcohol (IPA) solution at 0 $^{\circ}$C for 30 s. The developer solution was cooled using a thermoelectric cold plate with a stirring bar promoting homogeneous temperature distribution. The developed samples were dried using a nitrogen spray gun. After development, a 20 nm thick layer of Al was deposited by an e-beam evaporator (*Temescal FC*-2000) with the base pressure of $\sim 10^{-7}$ Torr. The Al deposition rate was kept as 10 Å s^{-1} (on a quartz crystal microbalance) to limit oxidation in the vacuum chamber. For the metal lift-off, the samples were immersed in n-methylpyrrolidone (NMP) heated at 60 $^{\circ}$C for $\sim$15 min and then rinsed by acetone and isopropanol, respectively.

4.2. TEM and EELS measurements

Bright-field TEM images were acquired using a *JEOL* 2100 LaB$_6$ TEM operated at 200 keV and a *FEI Titan* 80–300 keV FEG S/TEM operated at 80 keV. A non-monochromated *Nion UltraSTEM* operating at 60 keV was used for annular dark field imaging and EELS measurements. EELS energy resolution was $\sim$0.30 eV. EELS maps were extracted by summing over an energy window of 0.2 eV in the energy range of 1.0–20.48 eV. The zero-loss peak (ZLP) was modeled using various functions (see figure S17) and the model was used for the deconvolution of data using Richardson–Lucy (RL) algorithm with 3 iterations. After the RL deconvolution, the modeled ZLP was subtracted from the deconvoluted EEL spectra. We fitted the EELS data to a Lorentzian function to create the maps of width (FWHM), lifetime and peak positions.

4.3. BEM Simulations

Low-loss EELS simulations of Al nanocavities were carried out using a Matlab toolbox 'MNPBEM' based on BEM [76]. The LSPRs of Al-based nanostructures were previously modeled by full-wave Maxell electromagnetic simulations and finite-difference time-domain simulations [77, 78]. The dielectric functions of Al were taken from McPeak *et al* [79, 80]. The length, width and thickness of the rods were kept as 38 nm, 15 nm and 15 nm, respectively. After a geometrical mesh is used to discretize boundaries between the materials defined in the code, MNPBEM solves the Maxwell equations by means of these boundary conditions. For the simplicity of simulations, an effective medium approach was employed. Thus the existence of a SiN$_x$ membrane and an oxide layer covering Al nanorods were disregarded. An electron beam excitation with the electron beam width of 0.2 nm and beam energy of 60 keV was used in the simulations. BEM simulations of EEL spectra were performed at the energy range of 0.73–8.23 eV with 500 mesh.

Acknowledgments

and lithography equipment was provided through the Advanced Microscopy Laboratory. The authors acknowledge helpful discussions and technical support from Prof. Valeria Nicolosi, Prof John Boland, Dermot Daly, Dr Kamonpan Chumpol and Dr Niall McEvoy.

Data availability statement

All data that support the findings of this study are included within the article (and any supplementary files).

ORCID iDs

Kenan Elibol https://orcid.org/0000-0002-8765-2794
Richard G Hobbs https://orcid.org/0000-0003-0855-3710

References

[1] Phan A D, Le N B, Lien N T H and Wakabayashi K 2018 Multilayered plasmonic nanostructures for solar energy harvesting *J. Phys. Chem.* C **122** 19801–6

[2] Li G, Cherqui C, Bigelow N W, Duscher G, Straney P J, Millstone J E, Masiello D J and Camden J P 2015 Spatially mapping energy transfer from single plasmonic particles to semiconductor substrates via STEM/EELS *Nano Lett.* **15** 3465–71

[3] Zhao M *et al* 2016 Actively tunable visible surface plasmons in Bi2Te3 and their energy-harvesting applications *Adv. Mater.* **28** 3138–44

[4] Casanova D, Matxain J M and Ugalde J M 2016 Plasmonic resonances in the Al13− cluster: quantification and origin of exciton collectivity *J. Phys. Chem.* C **120** 12742–50

[5] Kale M J, Avanesian T and Christopher P 2014 Direct photocatalysis by plasmonic nanostructures *ACS Catal.* **4** 116–28

[6] Genevet P, Tetienne J-P, Gatzogiannis E, Blanchard R, Kats M A, Scully M O and Capasso F 2010 Large enhancement of nonlinear optical phenomena by plasmonic nanocavity gratings *Nano Lett.* **10** 4880–3

[7] Kauranen M and Zayats A V 2012 Nonlinear plasmonics *Nat. Photon.* **6** 737–48

[8] Gordon R 2022 Future prospects for biomolecular trapping with nanostructured metals *ACS Photon.* **9** 1127–35

[9] Xue L, Yamazaki H, Ren R, Wanunu M, Ivanov A P and Edel J B 2020 Solid-state nanopore sensors *Nat. Rev. Mater.* **5** 931–51

[10] Kim T, Kang S, Heo J, Cho S, Kim J W, Choe A, Walker B, Shanker R, Ko H and Kim J Y 2018 Nanoparticle-enhanced silver-nanowire plasmonic electrodes for high-performance organic optoelectronic devices *Adv. Mater.* **30** 1800659

[11] Lee Y H, Lee T K, Song I, Yu H, Lee J, Ko H, Kwak S K and Oh J H 2016 Boosting the performance of organic optoelectronic devices using multiple-patterned plasmonic nanostructures. *Adv. Mater.* **28** 4976–82

[12] Hobbs R G, Putnam W P, Fallahi A, Yang Y, Kärtner F X and Berggren K K 2017 Mapping photoemission and hot-electron emission from plasmonic nanoantennas *Nano Lett.* **17** 6069–76

[13] Knight M W, King N S, Liu L, Everitt H O, Nordlander P and Halas N J 2014 Aluminum for plasmonics *ACS Nano* **8** 834–40

[14] Ringe E 2020 Shapes, plasmonic properties, and reactivity of magnesium nanoparticles *J. Phys. Chem.* C **124** 15665–79

[15] Biggins J S, Yazdi S and Ringe E 2018 Magnesium nanoparticle plasmonics *Nano Lett.* **18** 3752–8

[16] Gutiérrez Y, Losurdo M, González F, Everitt H O and Moreno F 2020 Nanoplasmonic photothermal heating and near-field enhancements: a comparative survey of 19 metals *J. Phys. Chem.* C **124** 7386–95

[17] Elibol K and van Aken P A 2022 Hybrid graphene-supported aluminum plasmonics *ACS Nano.* (https://doi.org/ 10.1021/acsnano.2c01730)

[18] Gérard D and Gray S K 2014 Aluminium plasmonics *J. Phys. D: Appl. Phys.* **48** 184001

[19] Hao Q, Wang C, Huang H, Li W, Du D, Han D, Qiu T and Chu P K 2015 Aluminum plasmonic photocatalysis *Sci. Rep.* **5** 15288

[20] Ghori M Z, Veziroglu S, Hinz A, Shurtleff B B, Polonskyi O, Strunskus T, Adam J, Faupel F and Aktas O C 2018 Role of UV plasmonics in the photocatalytic performance of TiO2 decorated with aluminum nanoparticles *ACS Appl. Nano Mater.* **1** 3760–4

[21] King N S, Liu L, Yang X, Cerjan B, Everitt H O, Nordlander P and Halas N J 2015 Fano resonant aluminum nanoclusters for plasmonic colorimetric sensing *ACS Nano* **9** 10628–36

[22] Tanabe I, Tanaka Y Y, Watari K, Inami W, Kawata Y and Ozaki Y 2020 Enhanced surface plasmon resonance wavelength shifts by molecular electronic absorption in far- and deep-ultraviolet regions *Sci. Rep.* **10** 9938

[23] Liu H-W, Lin F-C, Lin S-W, Wu J-Y, Chou B-T, Lai K-J, Lin S-D and Huang J-S 2015 Single-crystalline aluminum nanostructures on a semiconducting GaAs substrate for ultraviolet to near-infrared plasmonics *ACS Nano* **9** 3875–86

[24] Shrestha V R, Lee S-S, Kim E-S and Choi D-Y 2014 Aluminum plasmonics based highly transmissive polarization-independent subtractive color filters exploiting a nanopatch array *Nano Lett.* **14** 6672–8

[25] Syrenova S, Wadell C and Langhammer C 2014 Shrinking-hole colloidal lithography: self-aligned nanofabrication of complex plasmonic nanoantennas *Nano Lett.* **14** 2655–63

[26] Arnob M M P, Zhao F, Li J and Shih W-C 2017 EBL-based fabrication and different modeling approaches for nanoporous gold nanodisks *ACS Photon.* **4** 1870–8

[27] Barrow S J, Collins S M, Rossouw D, Funston A M, Botton G A, Midgley P A and Mulvaney P 2016 Electron energy loss spectroscopy investigation into symmetry in gold trimer and tetramer plasmonic nanoparticle structures *ACS Nano* **10** 8552–63

[28] Haran G and Chuntonov L 2018 Artificial plasmonic molecules and their interaction with real molecules *Chem. Rev.* **118** 5539–80

[29] Mackin R T, Cohn B, Engelman B, Goldner A, Rubtsov I V and Chuntonov L 2019 Plasmonic trimers for dual-frequency surface-enhanced two-dimensional infrared spectroscopy *J. Phys. Chem.* C **123** 24731–9

[30] Satter S S, Mahdy M R C, Ohi M A R, Islam F and Rivy H M 2018 Plasmonic cube tetramers over substrates: reversal of binding force as the effect of fano resonance and light polarization *J. Phys. Chem.* C **122** 20923–34

[31] Weber W H and Ford G W 2004 Propagation of optical excitations by dipolar interactions in metal nanoparticle chains *Phys. Rev.* B **70** 125429

[32] Manfrinato V R, Camino F E, Stein A, Zhang L, Lu M, Stach E A and Black C T 2019 Patterning Si at the 1 nm length scale with aberration-corrected electron-beam lithography: tuning of plasmonic properties by design *Adv. Funct. Mater.* **29** 1903429

[33] Koh A L, McComb D W, Maier S A, Low H Y and Yang J K W 2010 Sub-10 nm patterning of gold nanostructures on silicon-nitride membranes for plasmon mapping with electron energy-loss spectroscopy *J. Vac. Sci. Technol.* B **28** C6O45–6O49

[34] Hobbs R G, Manfrinato V R, Yang Y, Goodman S A, Zhang L, Stach E A and Berggren K K 2016 High-energy surface and volume plasmons in nanopatterned sub-10 nm aluminum nanostructures *Nano Lett.* **16** 4149–57

[35] Nandi P, Sang X, Hoglund E R, Unocic R R, Molodov D A and Howe J M 2019 Nanoscale mapping of the electron density at Al grain boundaries and correlation with grain-boundary energy *Phys. Rev. Mater.* **3** 053805

[36] Yang H, Garfunkel E L and Batson P E 2020 Probing free carrier plasmons in doped semiconductors using spatially resolved electron energy loss spectroscopy *Phys. Rev.* B **102** 205427

[37] Slaughter L S, Wu Y, Willingham B A, Nordlander P and Link S 2010 Effects of symmetry breaking and conductive contact on the plasmon coupling in gold nanorod dimers *ACS Nano* **4** 4657–66

[38] Eschimèse D, Vaurette F, Ha C, Arscott S, Mélin T and Lévêque G 2022 Strong and weak polarization-dependent interactions in connected and disconnected plasmonic nanostructures *Nanoscale Adv.* **4** 1173–81

[39] Grzelczak M, Mezzasalma S A, Ni W, Herasimenka Y, Feruglio L, Montini T, Pérez-Juste J, Fornasiero P, Prato M and Liz-Marzán L M 2012 Antibonding plasmon modes in colloidal gold nanorod clusters *Langmuir* **28** 8826–33

[40] Zhang X, Zhang X, Luo C, Liu Z, Chen Y, Dong S, Jiang C, Yang S, Wang F and Xiao X 2019 Volume-enhanced raman scattering detection of viruses *Micro and Nano: No Small Matter* **15** 1805516

[41] Sreekanth K V, Alapan Y, ElKabbash M, Ilker E, Hinczewski M, Gurkan U A, De Luca A and Strangi G 2016 Extreme sensitivity biosensing platform based on hyperbolic metamaterials *Nat. Mater.* **15** 621–7

[42] Yu M, Huang Z, Liu Z, Chen J, Liu Y, Tang L and Liu G 2018 Annealed gold nanoshells with highly-dense hotspots for large-area efficient Raman scattering substrates *Sensors Actuators* B **262** 845–51

[43] Altug H, Oh S-H, Maier S A and Homola J 2022 Advances and applications of nanophotonic biosensors *Nat. Nanotechnol.* **17** 5–16

[44] Liu G, Liu Y, Tang L, Liu X, Fu G and Liu Z 2019 Semiconductor-enhanced Raman scattering sensors via quasi-three-dimensional Au/Si/Au structures *Nanophotonics* **8** 1095–107

[45] Xia C, Yin C and Kresin V V 2009 Photoabsorption by volume plasmons in metal nanoclusters *Phys. Rev. Lett.* **102** 156802

[46] Coyle S, Netti M C, Baumberg J J, Ghanem M A, Birkin P R, Bartlett P N and Whittaker D M 2001 Confined plasmons in metallic nanocavities *Phys. Rev. Lett.* **87** 176801

[47] Barrow S J, Rossouw D, Funston A M, Botton G A and Mulvaney P 2014 Mapping bright and dark modes in gold nanoparticle chains using electron energy loss spectroscopy *Nano Lett.* **14** 3799–808

[48] Lingstädt R *et al* 2020 Probing plasmonic excitation mechanisms and far-field radiation of single-crystalline gold tapers with electrons *Philos. Trans. R. Soc.* A **378** 20190599

[49] Smolyaninov I I 2008 Optical microscopy beyond the diffraction limit *HFSP J.* **2** 129–31

[50] Lauterbach M A 2012 Finding, defining and breaking the diffraction barrier in microscopy—a historical perspective *Opt. Nanoscopy* **1** 8

[51] Vesseur E J R, Aizpurua J, Coenen T, Reyes-Coronado A, Batson P E and Polman A 2012 Plasmonic excitation and manipulation with an electron beam *MRS Bull.* **37** 752–60

[52] Cai W, Sainidou R, Xu J, Polman A and García de Abajo F J 2009 Efficient generation of propagating plasmons by electron beams *Nano Lett.* **9** 1176–81

[53] Koh A L, Fernández-Domínguez A I, McComb D W, Maier S A and Yang J K W 2011 High-resolution mapping of electron-beam-excited plasmon modes in lithographically defined gold nanostructures *Nano Lett.* **11** 1323–30

[54] Chu M-W, Myroshnychenko V, Chen C H, Deng J-P, Mou C-Y and García de Abajo F J 2009 Probing bright and dark surface-plasmon modes in individual and coupled noble metal nanoparticles using an electron beam *Nano Lett.* **9** 399–404

[55] Steyskal E-M, Oberdorfer B, Sprengel W, Zehetbauer M, Pippan R and Würschum R 2012 Direct experimental determination of grain boundary excess volume in metals *Phys. Rev. Lett.* **108** 055504

[56] Bosman M, Zhang L, Duan H, Tan S F, Nijhuis C A, Qiu C W and Yang J K W 2014 Encapsulated annealing: enhancing the plasmon quality factor in lithographically–defined nanostructures *Sci. Rep.* **4** 5537

[57] Elibol K, Mangler C, Gupta T, Zagler G, Eder D, Meyer J C, Kotakoski J and Bayer B C 2020 Process pathway controlled evolution of phase and Van-der-Waals epitaxy in In/In2O3 on graphene heterostructures *Adv. Funct. Mater.* **30** 2003300

[58] Mecklenburg M, Hubbard W A, White E R, Dhall R, Cronin S B, Aloni S and Regan B C 2015 Nanoscale temperature mapping in operating microelectronic devices *Science* **347** 629

[59] Cherqui C, Li G, Busche J A, Quillin S C, Camden J P and Masiello D J 2018 Multipolar nanocube plasmon mode-mixing in finite substrates *J. Phys. Chem. Lett.* **9** 504–12

[60] Maiti A, Maity A and Chini T K 2015 Mode mixing and substrate induced effect on the plasmonic properties of an isolated decahedral gold nanoparticle *J. Phys. Chem.* C **119** 18537–45

[61] Gao Y, Zhou N, Shi Z, Guo X and Tong L 2018 Dark dimer mode excitation and strong coupling with a nanorod dipole *Photon. Res.* **6** 887–92

[62] Kollmann H *et al* 2014 Toward plasmonics with nanometer precision: nonlinear optics of helium-ion milled gold nanoantennas *Nano Lett.* **14** 4778–84

[63] Elibol K and van Aken P A 2022 Uncovering the evolution of low-energy plasmons in nanopatterned aluminum plasmonics on graphene *Nano Lett.* **22** 5825–31

[64] Tanaka I, Mizoguchi T, Sekine T, He H, Kimoto K, Kobayashi T, Mo S-D and Ching W Y 2001 Electron energy loss near-edge structures of cubic Si_3N_4 *Appl. Phys. Lett.* **78** 2134–6

[65] Gildenburg V B, Kostin V A and Pavlichenko I A 2016 Excitation of surface and volume plasmons in a metal nanosphere by fast electrons *Phys. Plasmas* **23** 032120

[66] Moreau P, Brun N, Walsh C A, Colliex C and Howie A 1997 Relativistic effects in electron-energy-loss-spectroscopy observations of the Si/SiO_2 interface plasmon peak *Phys. Rev.* B **56** 6774–81

[67] Egerton R F 2017 Scattering delocalization and radiation damage in STEM-EELS *Ultramicroscopy* **180** 115–24

[68] Krishan V and Ritchie R H 1970 Anomalous damping of volume plasmons in polycrystalline metals *Phys. Rev. Lett.* **24** 1117–9

[69] Wiener A, Duan H, Bosman M, Horsfield A P, Pendry J B, Yang J K W, Maier S A and Fernández-Domínguez A I 2013 Electron-energy loss study of nonlocal effects in connected plasmonic nanoprisms *ACS Nano* **7** 6287–96

[70] Abe H, Terauchi M, Kuzuo R and Tanaka M 1992 Temperature dependence of the volume-plasmon energy in aluminum *J. Electron Microsc.* **41** 465–8

[71] Barker A, Sapkota B, Oviedo J P and Klie R 2021 Automated plasmon peak fitting derived temperature mapping in a scanning transmission electron microscope *AIP Advances* **11** 035330

[72] Khosravi Khorashad L, Besteiro L V, Wang Z, Valentine J and Govorov A O 2016 Localization of excess temperature using plasmonic hot spots in metal nanostructures: combining nano-optical antennas with the fano effect *J. Phys. Chem.* C **120** 13215–26

[73] Kuppe C, Rusimova K R, Ohnoutek L, Slavov D and Valev V K 2020 'Hot' in plasmonics: temperature-related concepts and applications of metal nanostructures *Adv. Opt. Mater.* **8** 1901166

[74] Vovchuk D, Kosulnikov S, Noskov R E and Ginzburg P 2020 Wire resonator as a broadband Huygens superscatterer *Phys. Rev.* B **102** 094304

[75] Brucoli G and Martín-Moreno L 2011 Effect of defect depth on surface plasmon scattering by subwavelength surface defects *Phys. Rev.* B **83** 075433

[76] Hohenester U 2014 Simulating electron energy loss spectroscopy with the MNPBEM toolbox *Comput. Phys. Commun.* **185** 1177–87

[77] Yang Y, Hobbs R G, Keathley P D and Berggren K K 2020 Electron energy loss of ultraviolet plasmonic modes in aluminum nanodisks *Opt. Express* **28** 27405–14

[78] Chumpol K, McEvoy N, Zhang X and Hobbs R G 2020 Multiphoton absorption and graphitization in poly(methyl methacrylate)-coated aluminum nanoantenna arrays *J. Phys. Chem.* C **124** 8930–7

[79] McPeak K M, Jayanti S V, Kress S J P, Meyer S, Iotti S, Rossinelli A and Norris D J 2015 Plasmonic films can easily be better: rules and recipes *ACS Photon.* **2** 326–33

[80] Aleksandar D R 1995 Algorithm for the determination of intrinsic optical constants of metal films: application to aluminum *Appl. Opt.* **34** 4755–67